ADVANCED MATERIALS
www.advmat.de

Visible-Frequency Metasurface for Structuring and Spatially Multiplexing Optical Vortices

*M. Q. Mehmood, Shengtao Mei, Sajid Hussain, Kun Huang, S. Y. Siew, Lei Zhang, Tianhang Zhang, Xiaohui Ling, Hong Liu, Jinghua Teng, Aaron Danner, Shuang Zhang, and Cheng-Wei Qiu**

Optical phase singularities have been an enticing topic for both theoretical and applied researches over the last couple of decades after their discovery by Allen et al. in 1992.[1] It is now well-understood that the orbital angular momentum (OAM) can take an arbitrary value within a continuous range, either integer or noninteger, in the unit of $\hbar$ per photon ($\hbar$ is reduced Planck's constant).[2–4] These OAM-carrying beams are generally referred to as optical vortices (OVs), quantified by the helicity of the phase-front with an azimuthal angular dependence of $\exp(-im\theta)$, where "m" is the topological charge.[5] A prominent attribute of OVs is a phase singularity indicating a dark core with zero intensity along the beam-axis together with an annular transverse intensity profile. The discovery of OAM has significantly boosted the study of its intriguing properties and incubated an avenue of promising technological development in optical tweezers and spanners,[6,7] optical data storage,[8] nonlinear optics,[9] and quantum information processing.[10,11] Currently, various approaches have been demonstrated to generate vortex beams, such as spiral phase plates (SPPs),[12,13] computer-generated holograms,[14,15] cylindrical mode converter,[16,17] and Q-plates.[18] However, these conventional OV generators are bulky and hence restrict their employment in integrated optics. These restraints thus have inspired researchers to seek methods necessary to reduce the size of OV generators owing to the emerging OAM-based applications at miniature scales.[19–23]

Recently, an intriguing 2D metamaterial, called the metasurface,[24] has gained attention due to its ability to manipulate optical phase fronts. Instead of acquiring a desired phase change through propagation effect, it is capable of imparting a space-variant abrupt phase change on an incident electromagnetic wave via an ultrathin layer of nanostructured material. The idea revolutionized the concept of light control and paved the way toward the construction of a wide range of ultrathin optical devices and effects such as metalenses,[25,26] optical spin hall effect[27] and spin-controlled photonics,[28–30] nonperiodic photon sieves[31] quarter-wave-plates,[32] and devices capable of 3D optical holography.[33] Such phase-modification capability of the metasurface potentially allows significant reduction in the size of OV generators. In this regard, Yu et al.[24] and Genevet et al.[34] demonstrated the generation of OV beams via metasurfaces, where an interferometric approach was used to extract the spiral phase-fronts of the scattered vortex beam.

Their V-shaped nanorods responded to linearly polarized illumination, where anomalous refraction was obtained for cross-linearly polarized light. Besides this pioneering study, the concept of anomalous reflection/refraction was extended to circularly polarized (CP) illumination and spin–orbit interaction was exploited to achieve an ultrathin lens and SPP for cross-CP light.[35] In brief, these endeavors for achieving compact OV generators, based on metasurfaces, made use of ultrathin SPPs to achieve a helical beam for (anomalously refracted/reflected) linearly and circularly cross-polarized light.[34,35] However, those OV plates were restricted to create one specific topological charge for a fabricated device, whereas a separate device would be required (every time) to attain another topological charge.

Moreover, such devices yield a propagating OV instead of concentrated photons with a simultaneous well-defined focal plane, which is an essential ingredient for optical trapping and manipulation. Therefore, their applications (via single fabricated device) are seriously constrained when highly concentrated OVs with different topological charges are needed.

In this work, we employ the concept of a controllable interfacial phase discontinuity and combine the functionalities of two distinct optical devices, a lens and an SPP, into a single design to realize an ultrathin nanostructured OV generator with multiple focal planes along the longitudinal direction; whereas the number of focal planes, corresponding topological charges, and focal lengths can be readily tailored to meet different requirements. The polarization state (i.e., spin angular momentum)

Dr. M. Q. Mehmood, S. Mei, Dr. S. Hussain, S. Y. Siew, Dr. L. Zhang, T. Zhang, Dr. X. Ling, Prof. A. Danner, Prof. C.-W. Qiu
Department of Electrical and Computer Engineering
National University of Singapore
4 Engineering Drive 3, Singapore 117583
E-mail: chengwei.qiu@nus.edu.sg
S. Mei, Prof. C.-W. Qiu
Graduate School for Integrative Sciences and Engineering
National University of Singapore
Centre for Life Sciences (CeLS)
#05-01, 28 Medical Drive, Singapore 117456, Singapore
Dr. K. Huang, Dr. H. Liu, Dr. J. Teng
Institute of Materials Research and Engineering Agency for Science Technology and Research (A*STAR)
Innovis
#08-03, 2 Fusionopolis Way, Singapore 138634
Dr. X. Ling
College of Physics and Electronic Engineering
Hengyang Normal University
Hengyang 421002, China
Prof. S. Zhang
School of Physics & Astronomy
University of Birmingham
Birmingham B15 2TT, UK

DOI: 10.1002/adma.201504532

ADVANCED MATERIALS
www.advmat.de

Materials Views
www.MaterialsViews.com

and position of the focal planes can be controlled by manipulating the helicity of the incident light. Unlike traditional diffractive spiral phase and zone plates,[36] the proposed lens is ultrathin (60 nm), compact, and supports multiple focal planes. The presence of highly concentrated OVs with distinct topological charges at different longitudinal focal planes makes our ultrathin OV generators promising devices for optical manipulation at nanoscale dimensions.

Figure 1a depicts a schematic diagram of an inverted metasurface design built on Babinet's principle. Instead of metallic nanoantennas, we employ a set of similarly shaped nanovoids milled into a 60 nm thin Au film, where the length (l) and width (w) of each nanovoid are 150 and 75 nm, respectively. The main motive for employing the Babinet design is to attain higher signal-to-noise ratio (SNR) [SNR = 10 $\log_{10}$ (P_d/P_{ud}) dB] by increasing transmission of the desired power (P_d = cross-CP transmitted

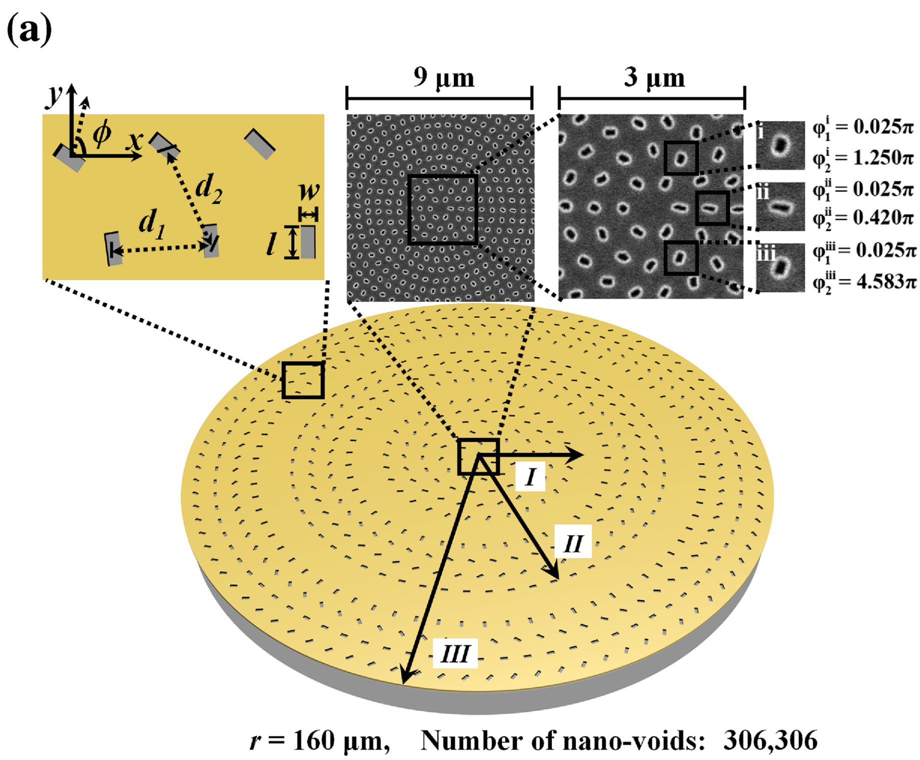

(b)

Detailed parameters and ranges of the proposed design			
	Region I	Region II	Region III
Radius	0.5 μm≤r_1≤40 μm	45 μm≤r_2≤100 μm	105 μm≤r_3≤160 μm
Focal plane	40 μm	100 μm	160 μm
Number of nano-voids	20,358	101,128	184,820
Radial rotation angle (φ_1) – Equation 1	[0, 82 π]	[48 π, 206 π]	[156 π, 329 π]
Azimuthal rotation angle (φ_2) – Equation 2	[0, 5 π]	[0, 4.0 π]	[0, 3.0 π]

Figure 1. Schematic diagram of the proposed metalens, SEM images and the detailed design parameters. a) Artistic depiction of the designed multi-focus OV lens, which consists of three sublenses marked by Region I, II, and III. All nanovoids are arranged in concentric circles and the orientations of individual nanovoids are dictated by the rotational angle (φ) provided in Equation (3), where φ_1 varies radially and φ_2 varies azimuthally. Top-right inset gives the SEM images, for lower and higher magnification, of the fabricated metalens. Three nanovoids in the same ring are selected to show the fact that φ_1 remains constant in a certain ring and whereas φ_2 varies azimuthally. Top-left inset illustrates the pixel-level details of the structure, where each nanobar is 150 nm long (l) and 75 nm wide (w). Meanwhile, d_1 represents the distance between two neighboring rods (in the same circle) while d_2 denotes the distance between two neighboring concentric circles. Both of them (d_1 and d_2) are taken as 500 nm in our case. b) Table giving the detailed design parameters and SEM image, depicting the rotation angles of φ_1 and φ_2. It explicates the fact that φ_1 remains same along one circle, whereas φ_2 changes azimuthally (depending on the value of m) for every nanovoid. The radii of inner, middle, and outer sublenses are 0.5 μm ≤ r_1 ≤ 40 μm, 45 μm ≤ r_2 ≤ 100 μm, and 105 μm ≤ r_3 ≤ 160 μm, respectively.

power) compared to the unwanted power (P_{ud} = co-CP transmitted power).[37] The abrupt phase-change can only be obtained for the scattered cross-CP light,[35] and it means that only the cross-CP light is the desired signal whereas the co-CP light is the noise.[37] Higher SNR means higher cross-CP light compared to the case of nanobars' metasurface.[35] For the periodicity of 500 nm in both radial (d_1) and azimuthal (d_2) directions, the calculated SNR for the original metallic nanobars design[35] at 632.8 nm is about –17 dB, while our nanovoids' design yields the SNR of about –4 dB, which is 13 dB higher. This is because optically thick Au film (60 nm) serves as an opaque plate to effectively prevent the direct transmission of the incident light. Hence, light can transmit through nanovoids only, which significantly decreases the background interference and increases the purity of desired cross-CP light.

Pragmatically, it is crucial that the phase change for cross-CP light can be altered smoothly from 0 to 2π. The individual orientation angle (ϕ) of a given nanovoid, with respect to the x-axis, controls the abrupt phase change of the cross-CP scattered light (i.e., handedness of the scattered CP-light is opposite to the incident CP-light). Figure S1 (Supporting Information) shows the calculated phase-shift from 0 to $7\pi/4$, for left-handed circularly polarized (LHCP) light, through varying the orientation of nanovoids (ranging from 0 to $7\pi/8$) under right-handed circularly polarized (RHCP) excitation at $\lambda = 632.8$ nm.

To create multifocus OAM metalens, nanovoids are arranged in concentric rings, with radially and azimuthally varying orientations, in three sublenses: inner, middle, and outer (marked by I, II, and III). Each sublens is able to focus incident collimated Gaussian beam into a vortex beam well-defined topological charge at a specific focal plane. In our design, the center of all the nanovoids is located on concentric circles, where "d_1" represents the distance between two neighboring nanovoids on the same concentric circle and "d_2" is the difference of the radii of two neighboring concentric circles as depicted in the inset of Figure 1a. Both the distances, d_1 and d_2, are taken as 500 nm. The radii of regions I, II, and III are taken as 0.5 µm ≤ r_1 ≤ 40 µm, 45 µm ≤ r_2 ≤ 100 µm, and 105 µm ≤ r_3 ≤ 160 µm, respectively, whereas a radial gap of 5 µm is introduced between the neighboring sublenses to get well-separated and distinguishable focal planes. As a design principle, the numerical aperture (NA) of each sublens is kept same (≈ 0.707) to acquire relatively comparable intensity profiles at each focal plane. The NA in our case is defined as $\mathrm{NA} = n \cdot \sin[\arctan(D2f)]$, where "$n$" represents the refractive index (n = 1 for our case), "f" is the focal length of the lens, and "D" represents the diameter of the lens.

In order to achieve the desired phenomenon of nanostructured multifocus OV plate, the ultrathin flat lensing surfaces should incorporate two distinct phase profiles for all regions (I, II, and III): a lens and a vortex plate; so that the secondary waves emerging from the metasurface can constructively interfere at the focal plane to produce the focused OV with specific topological charge. In this regard, the overall rotational angle (ϕ) of individual elements is calculated via following expressions

$$\varphi_1(r) = \pm 0.5 k_0 \left(\sqrt{r^2 + f^2} - |f| \right) \quad (1)$$

$$\varphi_2(r) = \pm 0.5 m \cdot \arctan(y/x) \quad (2)$$

$$\phi(r) = \varphi_1(r) + \varphi_2(r) \quad (3)$$

where "$k_0 = 2\pi/\lambda$" is the free-space wave vector and "r" represents the distance of nanovoid from the center of the lens. The inner (0.5 µm ≤ r_1 ≤ 40 µm), middle (45 µm ≤ r_2 ≤ 100 µm), and outer (105 µm ≤ r_3 ≤ 160 µm) sublenses contribute to the first (f_1 = 40 µm), second (f_2 = 100 µm), and third focal planes (f_3 = 160 µm), respectively. It is evident from Equation (3) that the inclusive rotation of nanovoids is basically a summation of two distinct phase profiles, i.e., a lens (φ_1) and a vortex plate (φ_2), which collectively govern the phenomenon of focused OV. Figure 1a (top-right inset) gives the scanning electron microscope (SEM) images, for lower and higher magnification, of the fabricated metalens. Three nanovoids are selected in the second ring of Region I to exhibit the fact that φ_1 remains same along one circle, whereas φ_2 changes azimuthally (depending on the value of m) for every nanovoid. The phase discontinuity for the positive polarity lenses for RHCP illumination along the radial direction is given in Figure S2 (Supporting Information). The detailed design parameters and their ranges are given in Figure 1b, where the ranges of radial angular rotations φ_1 of nanovoids for Region I, II, and III are [0, 82π], [48π, 206π], and [156π, 329π], respectively. Since the inner, middle, and outer sublenses are designed for m = 5, 4, and 3, respectively, so φ_2 varies as [0, 5π], [0, 4π], [0, 3π] for the Region I, II, and III, respectively. The "±" signs in front of expression of φ_1 and φ_2, in Equations (1) and (2), illustrate that the orientation angle depends on the helicity of the incident light beam, where "+" ("–") represents the sign of the phase-shift for the incident beam with RHCP (LHCP) and the transmitted beam with LHCP (RHCP). Hence it can be inferred from "±" signs in Equations (1) and (2) that the real image will be formed for RHCP illumination (LHCP detection) on the transmission side, whereas virtual image will exist for the LHCP illumination (RHCP detection) on the $Z < 0$ side.

The experimental setup for demonstration of the OV metalens is given in Figure S3 (Supporting Information). A linear polarizer (LP1) and a quarter wave-plate (QWP1) are placed in front of the sample to convert the incoming collimated beam from the helium–neon laser (HeNe Laser, Research Electro Optics, Inc., model number = 32413, λ = 632.8 nm, output power = 35.0 mW) into the desired circular polarization state for the illumination (although, the output power of our laser, stated in the specs, is 35 mW but due to using the fiber to shine the laser's output on the sample, the output power (after the fiber) reduces to ≈20 mW). The sample is mounted on a translational stage. To magnify the micronsized, donut-shaped intensity distribution, a microscope objective lens (100×) are positioned behind the sample, and then followed by another pair of linear polarizer (LP2) and quarter wave-plate (QWP2) to ensure that only scattered light with opposite handedness, to that of incident beam, is captured by the charge-coupled device (CCD).

At first, we characterize a sample in which all sublenses (inner, middle, and outer) have identical positive polarity (+). The measured intensity profiles and the corresponding interference patterns on the transmission side of the structure are provided in **Figure 2** for RHCP illumination (LHCP detection). The focal length of the specific sublens can be determined by gradually adjusting the distance between the objective lens and the structure and examining the optical intensity distribution at

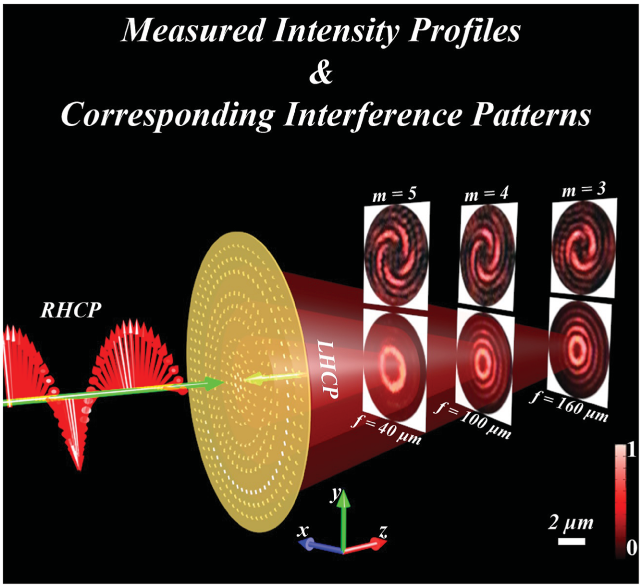

Figure 2. Measured intensity distribution and corresponding interference patterns at focal planes on the transmission side under RHCP illumination, where three real focal planes at $z = 40$, 100, and 160 μm are observed (for the cross circularly-polarized transmission: LHCP in this case) with the topological charges of $m = 5$, 4, and 3, respectively.

different z locations along the propagation direction. Three real focal planes are measured at f_1 = 40 μm, f_2 = 100 μm, and f_3 = 160 μm.

The corresponding topological charges of 5, 4, and 3 are confirmed from interference patterns. Since we employed the Pancharatnam–Berry (PB) phase metasurface, the detected vortex beams are formed by cross circularly polarized light, with respect to the incident circularly polarized light. However, the co-polarized light, without phase modulation, still exists in the output light, and it is filtered out by the circular polarizer during the detection process of focused vortex beams. If we deliberately let co-polarized light partially pass the filter by turning the polarizer, it will function as the reference spherical wave to interfere with the generated vortex beam (the cross-polarized light) to form the interference pattern. Confirmation of optical vortices via interference patterns corroborate the anticipated phenomenon of multifocus OAM with distinct topological charges.

Significantly, the sign of the abrupt phase change can be flipped by altering the helicity of incident light, which offers a unique flexibility to develop a multifocus lens under different CP illumination. In this regard, another OV metalens is designed with polarity for the middle sublens opposite to those for inner and outer sublenses. To achieve this purpose, the polarity of the middle lens is unchanged while the nanovoids' orientation angles for inner and outer regions are reversed as following

$$\varphi_1(r) = \mp\ 0.5k_0\left(\sqrt{r^2 + f^2} - |f|\right) \tag{4}$$

$$\varphi_2(r) = \mp\ 0.5m \cdot \arctan\left(y/x\right) \tag{5}$$

$$\phi(r) = \varphi_1(r) + \varphi_2(r) \tag{6}$$

Accordingly, the sign of phase shift generated by the metasurface is positive for the middle sublens while it is negative for the inner and outer sublenses under RHCP incident light. Therefore, there will be one real focal point at the location of second focal plane (for $Z > 0$), while two virtual focal points will appear at the locations of first and third focal planes (for $Z < 0$). When the helicity of the incident light is converted into LHCP, the polarities of all three sublenses will be switched, i.e., one virtual focal point at the location of second focal plane (for $Z < 0$) and two real focal points at the locations of first and third focal planes (for $Z > 0$) will emerge.

In order to experimentally verify the anticipated polarity switchable capability of the structure, we fabricated a separate sample with opposite neighboring polarities (but same focal lengths, i.e., f_1 = 40 μm, f_2 = 100 μm, and f_3 = 160 μm), where the middle sublens has "+" polarity while the inner and outer sublenses have "–" polarities. **Figure 3** shows CCD images for two different polarization-control configurations: RHCP/LHCP (illumination/detection) and LHCP/RHCP. For an RHCP illumination, Figure 3a elucidates that a donut-shaped intensity image, with $m = 4$, is observed at $Z = 100$ μm, which is a real focal plane and agrees well with the designed focal length. Since the inner and outer sublenses are fabricated for negative polarities (–), so the real images at first and third focal planes are invisible. However, two bright donut-shaped intensity profiles are observed at $Z = -40$ μm ($m = -5$) and $Z = -160$ μm ($m = -3$), which are virtual focal planes. The functioning of the lens reverses when LHCP light is shone on the structure, i.e., the middle sublens forms a virtual focal plane at $Z = -100$ μm ($m = -4$), while two real images are formed by the inner and outer sublenses at $Z = 40$ μm ($m = 5$) and $Z = 160$ μm ($m = 3$), respectively as given in Figure 3b. The conversion in the focusing properties from positive (negative) to negative (positive) is solely attributed to the handedness change of the CP incident light. The experimental results match the anticipation well.

Afterward, we experimentally investigate the response of same fabricated specimen to linearly polarized illumination. Due to the presence of LHCP and RHCP components with equal amplitudes, both real and virtual focal planes emerge simultaneously. As shown in **Figure 4**a, the corresponding results show that one real image at $Z = 100$ μm ($m = 4$) and two virtual images at $Z = -40$ μm ($m = -5$) and $z = -160$ μm ($m = -3$) are observed in the case of LHCP detection. For RHCP detection, Figure 4b illustrates that two real images are observed at Z= 40 μm ($m = 5$) and $Z = 160$ μm ($m = 3$), while a real image is detected at $z = 100$ μm ($m = 4$). Hence for the case of linearly polarized illumination, each sublens functions as a convergent and divergent lens simultaneously, which results in six focal planes (three real and three virtual) in total. The calculated transmission and conversion efficiencies for our case are ≈3.3% and ≈2%, respectively, which can be enhanced by increasing the density of the nanovoids.

Note that all three focal planes are well separated from each other. The dependence of focal distance on the incident wavelength, i.e., the extraordinary achromatic aberration, is a value-added merit of the proposed device. We can simply approximate the depth of the focus (DOF) of focused Laguerre Gaussian (LG) beams by employing $2\pi w_0^2/\lambda$ (where w_0 is the

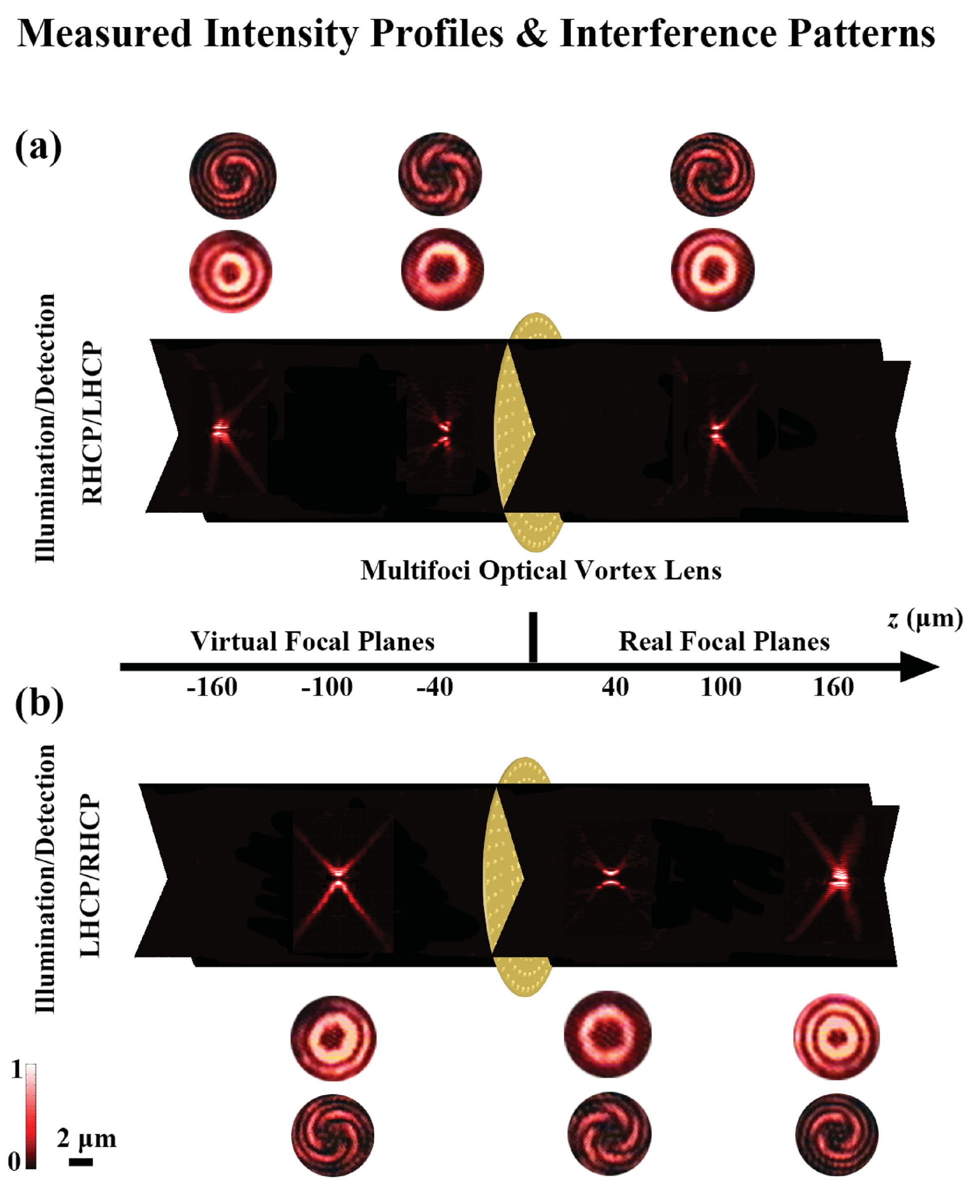

Figure 3. Measured intensity profiles (*xz*/*xy*-planes) and interference patterns (*xy*-planes) of multifocus OV lens (with positive polarity for sublens II and negative polarities for sublenses I and III). a) One real [at $z = 100$ μm ($m = 4$)] and two virtual focal planes [at $z = -40$ μm ($m = -5$) and $z = -160$ μm ($m = -3$)] are observed for RHCP illumination (LHCP detection). b) Two real [at $z = 40$ μm ($m = 5$) and $z = 160$ μm ($m = 3$)] and one virtual [at $z = -100$ μm ($m = -4$)] focal planes are observed for LHCP illumination (RHCP detection). Interference Patterns.

beam waist). The maximum radius of the intensity pattern on the focal plane is smaller than 2 μm. As a result, DOF is smaller than 40 μm. The distance between the neighboring two focal planes is 60 μm in our design, which is already much larger than the possible maximum DOF. Meanwhile, according to our measured results in Figures 3 and 4, it clearly shows that the separations between the focal planes are large enough (far beyond the nondiffracting range) to isolate different beams.

To summarize, we have experimentally demonstrated an ultrathin multifocus OV metalens, with distinct topological charges at each focal plane based on the Babinet-inverted nanovoids. Owing to the dual polarity feature of the phase response of nanovoids, the polarity of the proposed metalens can be readily altered between convergence and divergence by varying the helicity of incident light. The number of focal planes, their corresponding foci, and concomitant topological charges can be tailored to meet precise requirements of potential applications in nanoparticle manipulation. Our flat metalenses designs pave an innovative avenue to merge multiple bulk devices into a single ultrathin device to efficiently downsize photonic systems.

Experimental Section

Once the design was optimized through simulations, the desired lenses were specifically fabricated for three focal lengths: f_1 = 40 μm, f_2 = 100 μm, and f_3 = 160 μm, corresponding to an operational

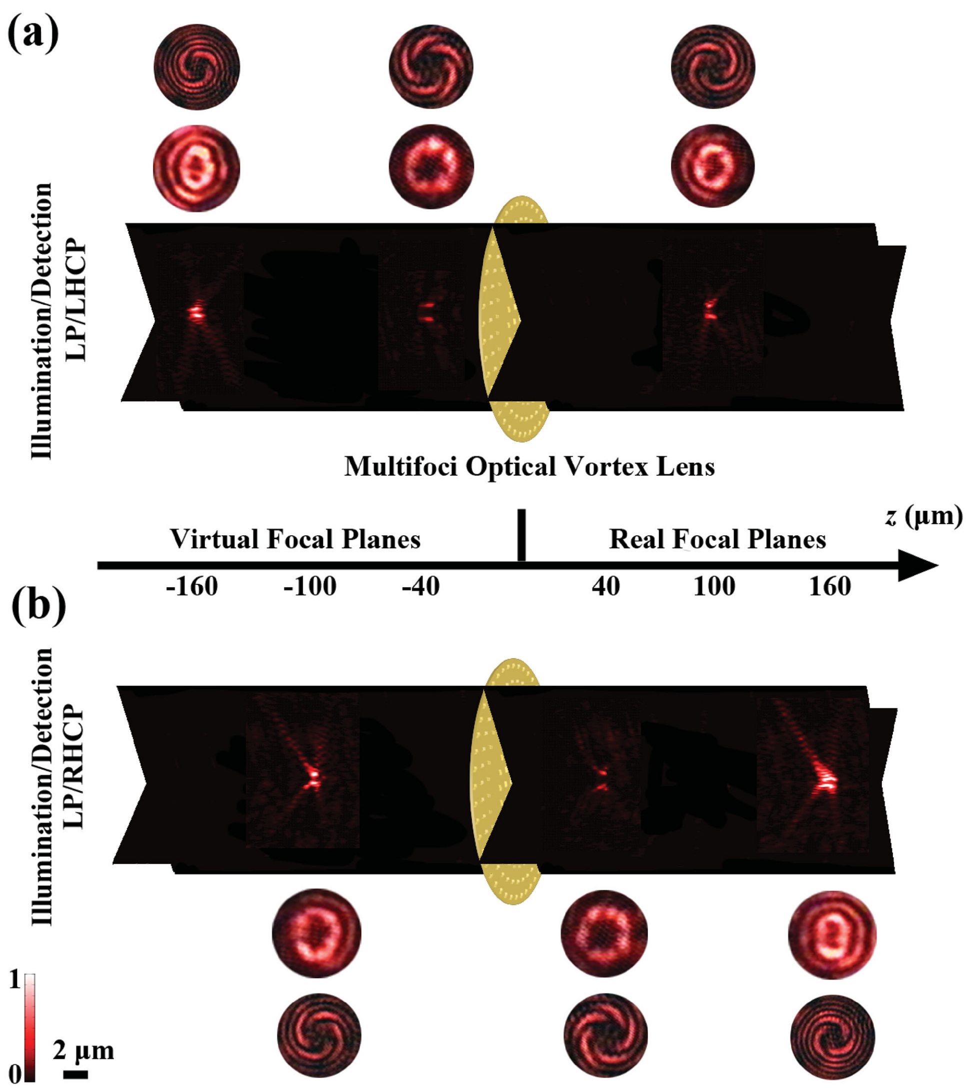

Figure 4. Measured intensity profiles (*xz*/*xy*-planes) and corresponding interference patterns of the multifocus OV lens (with positive polarity for sub-lens II and negative polarities for sub-lenses I and III) under LP illumination. a) One real [at $z = 100$ µm ($m = 4$)] and two virtual focal planes [at $z = -40$ µm ($m = -5$) and $z = -160$ µm ($m = -3$)] are observed for LP illumination (LHCP detection). b) Two real [at $z = 40$ µm ($m = 5$) and $z = 160$ µm ($m = 3$)] and one virtual [at $z = -100$ µm ($m = -4$)] focal planes are observed for LP illumination (RHCP detection).

wavelength of 632.8 nm. At first, a 60 nm thick Au-film, which was merely ≈1/10 of the working wavelength, was deposited onto a quartz substrate by electron-beam vapor deposition (Denton Vacuum, Explorer) at room temperature under a vacuum pressure of 5×10^{-7} Torr. Afterwards, the sample was coated with positive resist (PMMA 950K A11), having mixed with anisole (1:3 ratio), via spin-coater (6000 rpm for 45 s) to achieve the suitable thickness which could withstand against the milling process. The coated sample was then baked at the hotplate for 2 min at 180 °C. Electron beam lithography (eLine Plus, Raith) was subsequently performed to pattern the structure onto the resist by exposing the specimen at a dosage of 280 µC cm^{-2}, beam current of 47 pA and with an acceleration voltage of 20 kV. Once patterned, the structure was developed for 40 s in MIBK:IPA = 1:3. The specimen was then subjected to an argon ion beam etching process (Nanoquest, Intlvac) under conditions of acceleration voltage of 45 V, beam voltage of 300 V, beam current of 110 mA, and RF power of 170 W for ≈2 min. Eventually, 60 nm deep nanovoids (milled into Au-film) with feature dimensions of $l \times w$ = 150 nm × 75 nm were formed on the quartz substrate. The right-top inset of Figure 1a depicts SEM image of the fabricated metasurface lens.

Supporting Information

Supporting Information is available from the Wiley Online Library or from the author.

Acknowledgements

M.Q.M., S.M., and S.H. contributed equally to this work. This research was supported by the National Research Foundation, Prime Minister's Office, Singapore under its Competitive Research Program (CRP Award No. NRF-CRP10-2012-04). The project was partly supported by the Singapore National Research Foundation under the 10 Tb/in2 density storage project under CRP Award No. NRF-CRP4-2008-06. C.-W.Q. acknowledges the partial support from National University of Singapore (Grant No. R-263-000-A45-112). T.J. acknowledges Agency for Science, Technology and Research (A*STAR) under grant number 0921540099 and the A*STAR-MINDEF JFP under grant number 102 1740172. S.Z. acknowledges the support by the EPSRC (EP/J018473/1) and the Leverhulme Trust (RPG-2012-674), and the Royal Society.

Received: September 15, 2015
Revised: December 2, 2015
Published online: February 2, 2016

[1] L. Allen, M. W. Beijersbergen, R. J. C. Spreeuw, J. P. Woerdman, *Phys. Rev. A* **1992**, *45*, 8185.
[2] S. Orlov, K. Regelskis, V. Smilgevicius, A. Stabinis, *Opt. Commun.* **2002**, *209*, 155.
[3] J. Leach, E. Yao, M. J. Padgett, *New J. Phys.* **2004**, *6*, 71.
[4] K. Huang, H. Liu, M. Q. Mehmood, S. Mei, A. Danner, J. Teng, C. W. Qiu, *arXiv:1504.01909* **2015**.
[5] M. Y. Alison, J. P. Miles, *Adv. Opt. Photonics* **2011**, *3*, 161.
[6] E. M. Justin, J. P. Miles, *Contemp. Phys.* **2002**, *43*, 241.
[7] P. Miles, B. Richard, *Nat. Photonics* **2011**, *5*, 343.
[8] R. J. Voogd, M. Singh, J. J. M. Braat, *Opt. Data Storage* **2004**, *5380*, 387.
[9] D. S. Ding, Z. Y. Zhou, B. S. Shi, X. B. Zou, G. C. Guo, *Opt. Lett.* **2012**, *37*, 3270.
[10] V. D'Ambrosio, E. Nagali, L. Marrucci, F. Sciarrino, *Quantum Opt. II* **2012**, *8440*, 84400(F-1-11).
[11] X. B. Zou, W. Mathis, *Phys. Rev. A* **2005**, *71*, 042324.
[12] K. Sueda, G. Miyaji, N. Miyanaga, M. Nakatsuka, *Opt. Express* **2004**, *12*, 3548.
[13] G. A. Turnbull, D. A. Robertson, G. M. Smith, L. Allen, M. J. Padgett, *Opt. Commun.* **1996**, *127*, 183.
[14] N. R. Heckenberg, R. Mcduff, C. P. Smith, A. G. White, *Opt. Lett.* **1992**, *17*, 221.
[15] J. Arlt, K. Dholakia, L. Allen, M. J. Padgett, *J. Mod. Opt.* **1998**, *45*, 1231.
[16] M. Beijersbergen, L. Allen, H. Van, *Opt. Commun.* **1993**, *96*, 123.
[17] M. Padgett, L. Allen, *J. Opt. B: Quantum Semiclass. Opt.* **2002**, *4*, S17.
[18] K. Ebrahim, B. Piccirillo, E. Nagali, L. Marrucci, E. Santamato, *Appl. Phys. Lett.* **2009**, *94*, 231124.
[19] Y. Gorodetski, A. Niv, V. Kleiner, E. Hasman, *Phys. Rev. Lett.* **2008**, *101*, 043903.
[20] Y. Gorodetski, N. Shitrit, I. Bretner, V. Kleiner, E. Hasman, *Nano Lett.* **2009**, *9*, 3016.
[21] H. Liu, M. Q. Mehmood, K. Huang, L. Ke, H. P. Ye, P. Genevet, M. S. Zhang, A. Danner, S. P. Yeo, C. W. Qiu, J. H. Teng, *Adv. Opt. Mater.* **2014**, *2*, 1193.
[22] H. Kim, J. Park, S. W. Cho, S. Y. Lee, M. Kang, B. Lee, *Nano Lett.* **2010**, *10*, 529.
[23] Y. Gorodetski, A. Drezet, C. Genet, T. W. Ebbesen, *Phys. Rev. Lett.* **2013**, *110*, 203906.
[24] N. Yu, P. Genevet, M. A. Kats, F. Aieta, J. P. Tetienne, F. Capasso, Z. Gaburro, *Science* **2011**, *334*, 333.
[25] X. Z. Chen, L. L. Huang, H. Mühlenbernd, G. X. Li, B. F. Bai, Q. F. Tan, G. F. Jin, C. W. Qiu, S. Zhang, T. Zentgraf, *Nat. Commun.* **2012**, *3*, 1198.
[26] F. Aieta, P. Genevet, M. A. Kats, N. F. Yu, R. Blanchard, Z. Gahurro, F. Capasso, *Nano Lett.* **2012**, *12*, 4932.
[27] X. B. Yin, Z. L. Ye, J. Rho, Y. Wang, X. Zhang, *Science* **2013**, *339*, 1405.
[28] N. Shitrit, I. Yulevich, E. Maguid, D. Ozeri, D. Veksler, V. Kleiner, E. Hasman, *Science* **2013**, *340*, 724.
[29] G. X. Li, M. Kang, S. M. Chen, S. Zhang, E. Y. B. Pun, K. W. Cheah, J. S. Li, *Nano Lett.* **2013**, *13*, 4148.
[30] L. L. Huang, X. Z. Chen, B. F. Bai, Q. F. Tan, G. F. Jin, T. Zentgraf, S. Zhang, *Light Sci. Appl.* **2013**, *2*, e70.
[31] K. Huang, H. Liu, F. J. Garcia-Vidal, M. H. Hong, B. Luk'yanchuk, J. H. Teng, C. W. Qiu, *Nat. Commun.* **2015**, *6*, 7059.
[32] N. F. Yu, F. Aieta, P. Genevet, M. A. Kats, Z. Gaburro, F. Capasso, *Nano Lett.* **2012**, *12*, 6328.
[33] L. L. Huang, X. Z. Chen, H. Mühlenbernd, H. Zhang, S. M. Chen, B. F. Bai, Q. F. Tan, G. F. Jin, K. W. Cheah, C. W. Qiu, J. S. Li, T. Zentgraf, S. Zhang, *Nat. Commun.* **2013**, *4*, 2808.
[34] P. Genevet, N. Yu, F. Aieta, J. Lin, M. A. Kats, R. Blanchard, M. O. Scully, Z. Gaburro, F. Capasso, *Appl. Phys. Lett.* **2012**, *100*, 013101.
[35] L. Huang, X. Chen, H. Mühlenbernd, G. Li, B. Bai, Q. Tan, G. Jin, T. Zentgraf, S. Zhang, *Nano Lett.* **2012**, *12*, 5750.
[36] A. Sakdinawat, Y. Liu, *Opt. Lett.* **2007**, *32*, 2635.
[37] X. Ni, S. Ishii, A. V. Kildishev, V. M. Shalaev, *Light Sci. Appl.* **2013**, *2*, e72.